Brain Topography manuscript No.
(will be inserted by the editor)

Influence of a silastic ECoG grid on EEG/ECoG based source analysis

Benjamin Lanfer · Christian Röer · Michael Scherg · Stefan Rampp · Christoph Kellinghaus · Carsten Wolters

Received: date / Accepted: date

Abstract The simultaneous evaluation of the local electrocorticogram (ECoG) and the more broadly distributed electroencephalogram (EEG) from humans undergoing evaluation for epilepsy surgery has been shown to further the understanding of how pathologies give rise to spontaneous seizures. However, a

B. Lanfer
Westfälische Wilhelms-Universität Münster
Institute for Biomagnetism and Biosignalanalysis
Malmedyweg 15, 48149 Münster, Germany
Tel.: +49-251-8352413
Fax: +40-251-8356874
E-mail: benjamin.lanfer@uni-muenster.de

C. Röer
Westfälische Wilhelms-Universität Münster
Institute for Biomagnetism and Biosignalanalysis
Malmedyweg 15, 48149 Münster, Germany

M. Scherg
BESA GmbH
Freihamer Str. 18, 82166 Gräfelfing, Germany

S. Rampp
Epilepsy Center, Department of Neurology
University Hospital Erlangen, Erlangen, Germany

C. Kellinghaus
Department of Neurology
Klinikum Osnabrück, Osnabrück, Germany

C. H. Wolters
Westfälische Wilhelms-Universität Münster
Institute for Biomagnetism and Biosignalanalysis
Malmedyweg 15, 48149 Münster, Germany

well-known problem is that the disruption of the conducting properties of the brain coverings can render simultaneous scalp and intracranial recordings unrepresentative of the habitual EEG. The ECoG electrodes for measuring the potential on the surface of the cortex are commonly embedded into one or more sheets of a silastic material. These highly resistive silastic sheets influence the volume conduction and might therefore also influence the scalp EEG and ECoG measurements.

We carried out a computer simulation study to examine how the scalp EEG and the ECoG, as well as the source reconstruction therefrom, employing equivalent current dipole (ECD) estimation methods, are affected by the insulating ECoG grids. The finite element method (FEM) with high quality tetrahedral meshes, generated using a Constrained Delaunay Tetrahedralization (CDT) meshing approach, was used to model the volume conductor that incorporates the very thin ECoG sheets.

It is shown that the insulating silastic substrate of the ECoG grids can have a large impact on the scalp potential and on source reconstruction from scalp EEG data measured in the presence of the grids. The reconstruction errors are characterized with regard to the location of the source in the brain and the mislocalization tendency. In addition, we found a non-negligible influence of the insulating grids on ECoG based source analysis.

We conclude, that the thin insulating ECoG sheets should be taken into account, when performing source analysis of simultaneously measured ECoG and scalp EEG data.

Keywords Finite element method · FEM · ECoG · Presurgical epilepsy diagnosis · simultaneous EEG · constrained Delaunay tetrahedralization · dipole fitting method

1 Introduction

Epilepsy is a disorder affecting over 50 million people worldwide. A large group of those patients can be treated successfully using anti-epileptic drugs, but approx. 30% of the patients are pharmacoresistant [31]. An alternative effective treatment is the surgical resection of the epileptogenic tissue [43, 71]. The precise localization of the epileptogenic foci, preferably with non-invasive methods, is the major goal of the presurgical evaluation [50]. In addition to evaluation by video and electroencephalography (EEG) long-term monitoring, magnetic resonance imaging (MRI), single photon emission computed tomography and neuropsychological examination, source analysis of ictal or inter-ictal brain activity using EEG and magnetoencephalography (MEG) is a promising tool [51,21,36,23,14,55,69,25,65,4,3,53,45,52]. Source analysis results correlated well with results from intracranial electrocorticographic (ECoG) recordings [51,36,25,52] and epileptogenic subcompartments could well be distinguished using source reconstruction techniques [51,6,14,29]. In a large study, source analysis revealed additional localizational information in

35% of the 455 patients and in 10%, it could even contribute to the decision about type, size and eventually necessary prior invasive examinations [65].

In EEG and MEG source analysis the aim is to reconstruct the location and orientation of the sources of neurological activity from measured EEG or MEG data. Numerous methods have been proposed for this source reconstruction (e.g., [19,37]). Equivalent current dipole estimation (ECD) methods, like the dipole fitting method [56,39] or the goal-function scan method [39,24], are among the most widely used approaches.

Source reconstruction from EEG or ECoG data requires an appropriate solution of the so-called forward problem, that is, the estimation of the electric potentials from an assumed current density distribution. Different methods were proposed to solve the forward problem, analytic formulas assuming a spherical volume conductor geometry [40] being the earliest. In more recent times, numerical methods, for example, the boundary element method (BEM) [26], the finite difference method (FDM) [18], the finite volume method (FVM) [11], and the finite element method (FEM) [7,10,47,76,46] were developed to solve the EEG forward problem in realistic models of the human head. The FEM is known for its flexibility with regard to the geometry and conductivity distribution of the volume conductor model, so that it does not require simplifying assumptions on geometry or conductivities [58]. Thus, in combination with a suitable meshing approach, it is able to treat arbitrarily complex geometries and conductivity distributions, and it is therefore adequate for solving the forward problem in head volume conductors incorporating only fractions of a millimeter thin, highly insulating ECoG grids.

In the last years, there is an increasing interest in simultaneous intracranial and extracranial recordings of epileptiform activity [28,22,27,77,67,66, 48]. A problem of ECoG measurements is the uncertainty of the placement of the electrode grid in combination with the limited field-of-view of the ECoG electrodes. This problem can be alleviated by simultaneously measuring and analyzing the scalp EEG. For example, in a situation where only electrodes at the border of the ECoG grid pick up activity, source reconstruction from scalp EEG can be performed to verify that the ECoG grid is correctly placed above the origin of the recorded activity. Using the scalp EEG it is also possible to scan for activity in brain areas not covered by the ECoG grid, thus, for example, helping to decide if the activity detected in the ECoG originates from the seizure onset zone or if it already propagated there.

In addition, simultaneous measurement and evaluation of the local ECoG and the more broadly distributed EEG from humans undergoing evaluation for epilepsy surgery provides an opportunity to investigate the network dynamics of the epileptogenic brain. Evaluating both modalities sources immediately below the grid and in distant cortical and subcortical areas can be measured, and interactions between these sources can be revealed.

There is, however, a problem with simultaneous measurements of the ECoG and the scalp EEG. The ECoG measurement is performed using electrodes which are commonly embedded into one or more silastic sheets. These thin silastic sheets are highly insulating and might therefore influence the volume

conduction of the brain electric currents and, as a consequence, also affect the scalp EEG and ECoG measurements and the source analysis results therefrom. Such a disruption of the conducting properties of the brain coverings by ECoG grids can make simultaneous scalp and intracranial recordings unrepresentative of the habitual EEG [9,2,77,66].

Thus, an important research question is how exactly EEG and ECoG are influenced by the presence of the insulating grids, and also how source reconstruction based on EEG or ECoG data is affected.

Previous work on this was done by Zhang et al. [77]. In a simulation study they found a strong influence of insulating ECoG sheets on the scalp potential and on cortical potential imaging (CPI) from scalp EEG data.

Further publications with relevance for the topics of ECoG and source analysis exist [78,15,13]. Zhang et al. [78] investigated how current density reconstruction (CDR) methods can be used to perform source analysis based on ECoG data. Fuchs et al. [15] compared different volume conductor models for EEG and ECoG source analysis. The work of Dümpelmann et al. [13] is concerned with the application of minimum norm [20] and MUSIC [39] source reconstruction methods to ECoG data.

In this article, a simulation study is performed to investigate the influence of highly insulating ECoG grids on source analysis from the ECoG data itself and from simultaneously measured scalp EEG data. Potential distributions on the scalp and inside of the volume conductor are compared while ignoring, respectively, incorporating the insulating ECoG grids. Furthermore, to the best of our knowledge, it is studied for the first time how source reconstruction from scalp EEG and ECoG data by means of the widely-used ECD estimation approaches are affected by the presence of the insulating ECoG grids. Localization errors and mislocalization trends are assessed for a large number of probe sources distributed throughout the whole brain. Thus, we are able to make a statement, how much sources in brain regions closer to and more distant from the insulating grids are affected. In detailed, highly resolved error maps mislocalization trends and maximally affected dipole orientations are presented. Our study extends the work of Zhang et al. [77] with regard to the following important aspects: We investigate the influence of the silastic electrode sheets on source reconstruction using the widely-used ECD estimation method, allowing us to explicitly state which localization errors have to be expected when ignoring the grids. In addition, we study the influence on source analysis from ECoG data, and we investigate the influence for sources distributed throughout the whole brain.

In the context of our simulation study, we furthermore describe an alternative way of solving the forward problem in the complex volume conductor incorporating the thin, insulating ECoG sheets. The FEM and problem-adapted, high-quality CDT finite element meshes are used to model the electric properties of the head incorporating the thin silastic ECoG sheets. Advantages of the described method include good expected numerical convergence properties and the ability to model the ECoG grids without simplifying assumptions on the thickness of the grids.

2 Methods

2.1 The bioelectric forward and inverse problem

The problem of simulating the potential differences Φ from an assumed current density distribution J_p is called the bioelectric forward problem. Following [54, 19], a mathematical description for this problem is given by the quasi-static approximation of the Maxwell equations,

$$\nabla \cdot (\sigma \nabla \Phi) = J_p \text{ in } \Omega, \quad \langle \sigma \nabla \Phi, \mathbf{n} \rangle = 0 \text{ on } \Gamma \tag{1}$$

with σ being the tissue conductivity, $\Gamma = \partial\Omega$ the surface of the head domain Ω, $\langle \cdot, \cdot \rangle$ the scalar product and $\mathbf{n}$ the surface normal.

The non-uniqueness of the bioelectric inverse problem, that is, the estimation of J_p from measured potentials Φ, implies that assumptions on the source model, as well as anatomical and physiological a-priori knowledge about the source region should be taken into account to obtain a unique solution [54, 19]. Therefore, different inverse approaches for continuous and discrete source parameter space have been proposed (see, e.g., [19, 37] and the references therein). For the present study equivalent current dipole (ECD) estimation approaches are used to solve the inverse problem. The classical dipole fitting approach [56, 39] is employed for solving the inverse problem based on the EEG data. The optimization of the non-linear location parameters is performed using a Nelder-Mead simplex algorithm. Starting from an initial guess or seed point, the simplex algorithm finds the next local minimum of the cost function. To reliably find also the global minimum the simplex fit is repeatedly started from appropriately chosen seed points. For the dipole fits in the presented simulation study 16 different initial seed points distributed beneath the ECoG grids were used. Due to the limited field of view of the ECoG electrodes and a resulting more complex cost-function, we applied a goal function scan approach [39, 24] for ECD estimation from the ECoG data. In this approach, a single dipole is placed successively at each node of a scanning grid and the best fitting dipole moment is determined by linear estimation. In this way, for each grid node a goal function value is computed. The position of the grid node with the highest goal function value is interpreted as the reconstructed source position. A high resolution of the goal function scan is achieved by using a fine $1,\mathrm{mm}$ scanning grid.

2.2 Finite element method for the numerical solution of the forward problem

For volume conductors with arbitrary geometry and conductivity distribution equation (1) can be solved numerically using the FEM. To do so, the head domain is discretized into small elements, such as hexahedra or tetrahedra. In these elements the electric potential is approximated using polynomial basis functions. Among a variety of finite element approaches to model the dipole sources we chose the Venant direct method [10, 73] for our simulations because

it was shown in previous studies that it yields a good trade-off between accuracy and speed [33,73]. Employing standard variational techniques the finite element system of equations

$$\mathbf{K} \cdot \mathbf{u} = \mathbf{J} \tag{2}$$

can be derived from equation (1) [10,73]. In this linear equation system, $\mathbf{K} \in \mathbb{R}^{n \times n}$ is the stiffness matrix, with n being the number of finite element nodes, $\mathbf{u} \in \mathbb{R}^n$ is the discrete potential vector, containing an approximation to the potential at the finite element nodes, and $\mathbf{J} \in \mathbb{R}^n$ is the current vector. The number of finite element nodes, n, is typically a large number. Despite its size, $\mathbf{K}$ can easily be stored in memory on a common computer, because it is sparse, with only very few non-zero elements per column. In contrast, during inversion using a conventional direct solver, the decomposition of the matrix $\mathbf{K}$ would fill up and could not be stored in memory any longer. Therefore, to solve Equation (2) for a given right-hand side we use an iterative solver [75].

As described later, our study will necessitate thousands of single dipole fits and thus hundreds of thousands of forward computations, which would be practically impossible in combination with the FE forward approach when iteratively solving equation (2) for each of the source locations proposed by the nonlinear optimizer. Our investigation is enabled by means of a transfer matrix approach [70,75]. In this way, the large FE system of equations does not have to be solved for every source, which shall be simulated, but only $(s-1)$ times, where s is the number of sensors. After this setup step, the forward simulation for a single source using the Venant approach can then be performed in few milliseconds on a common PC.

For the computation of the transfer matrix, we employed an algebraic multigrid preconditioned conjugate gradient (AMG-CG) method, and for each sensor, we solved up to a relative error of 10^{-6} in the controllable $\mathbf{K}\mathbf{C}^{-1}\mathbf{K}$-energy norm (with $\mathbf{C}^{-1}$ being one V-cycle of the AMG) [33]. Using the AMG-CG solver the computation of the transfer matrix for 30 electrodes and the FE mesh used in this study with approximately 110k nodes takes only around 1 min 41 s on a common PC.

2.3 Accuracy aspects of the chosen numerical forward and inverse approaches

The complexity of the investigated volume conductor incorporating the very thin and highly insulating ECoG sheets raises the question how we can ensure that our FEM simulations achieve good numerical accuracies. This section is dedicated to the discussion of this question.

The FE method is deeply understood with regard to convergence aspects, even quantitative convergence proofs of the following form can be carried out [8, equation (7.1), Chapter 7]:

$$\|\Phi - \Phi_h\|_m \leq C \cdot h^k \tag{3}$$

with $\|\cdot\|_m$ being the H^m Sobolev norm [8, Definition 1.2], Φ the potential from equation (1) that we are searching for, $\Phi_h = \sum_{i=1}^{n} \varphi_i u_i$ the computed finite

element approximation with φ_i an FE basis function, h denotes the edge length of a finite element, C is a constant that is independent of h and reflects the mesh-regularity and k is the quantitative convergence order. In the following, we discuss the interplay of m, k, h and C and how we chose the parameters, especially h, to adapt the FE mesh to our specific problem.

In general, the order k depends on the regularity of the solution, on the degree of the FE basis functions, on the chosen Sobolev norm m, and on the approximation properties of the triangulation to the geometry [8, Chapter 7]. Because of the limited regularity of Φ in volume conductors with discontinuous conductivities (Φ is bending at tissue boundaries so that the resulting current density is continuous), we can only assume Φ to be in Sobolev space H^1 [76]. We therefore choose linear FE basis functions, so that we will not find a much higher convergence order than $k = 1$ for the Sobolev norm $m = 1$ (see [76], section 3.7). Therefore, for the investigated problem, it is advisable to use a small, problem-adapted and locally varying mesh-size h in combination with linear basis functions φ_i, as we have done here, instead of using higher order basis functions in combination with larger h which would end up in less accurate solutions for the same computational amount of work. Small h is needed especially in areas of large potential gradients or where an exact representation of the tissue structures needs full resolution. We therefore use highest resolution in the area of the 0.127 mm thin silastic grid (we especially take care that the grids are modeled without any holes) and lower resolution in areas where high-adaptivity is less advantageous.

On the other side, naive local mesh refinement leads to irregular tetrahedra in the border area between finely and coarsely meshed regions. Our meshing approach can partly compensate for this by only gradually changing the mesh resolution. But still, a very high mesh-resolution in the area of the silastic sheet and a much coarser mesh in other areas can only be achieved at the cost of a slightly increased mesh-irregularity. The constant C is affected by, amongst other factors, the regularity of the mesh [8, 17, 76]. However, for a finite size of C, we can always find an h so that the right-hand side of the equation (3) is small so that convergence of the approximative FE solution Φ_h to Φ is given.

In summary, the above convergence formula (3) tells us that we have to do our best to balance between a sufficiently small mesh size h that is adapted to accurately represent the potential function and a small constant C. Then, convergence is given through the above formula.

Furthermore, our experience from studies in multi-layer sphere models shows that the chosen FE forward modeling approach [33] as well as the inverse dipole fitting scenarios [72] achieve good numerical accuracy. In the latter work, dipole fitting localization errors were below 2 mm for all sources with eccentricities up to 1 mm below the cerebrospinal fluid (CSF) compartment in a model with a similar number of finite element nodes.

2.4 Adaptive constrained Delaunay tetrahedral meshing approach

For our simulation study the Constrained Delaunay Tetrahedralization (CDT) meshing approach [60,62] was employed for the generation of a tetrahedral finite element mesh that provides a good balance between locally refined mesh size h and small C. The meshing procedure starts with the preparation of a suitable boundary discretization of the segmented volume conductor compartments. Triangle meshes of the different tissue boundaries are produced that do not intersect each other. The absence of intersections is a necessary requirement for the input surfaces. The CDT approach is then used to construct a tetrahedralization conforming to the input surface meshes. This conformity is not guaranteed when using an ordinary Delaunay tetrahedralization. The CDT is constructed to fulfill two additional constraints to the size and shape of the tetrahedra. The first constraint restricts the volume of the generated tetrahedra (and thus h) in specified compartments, the so-called volume constraint. In our mesh, a very low volume constraint is chosen in the region of the insulating grids to adequately model the strong potential gradient due to the highly insulating ECoG grids. To keep C in a reasonable limit, the second constraint demands tetrahedra with a quality number Q lower than a given value, where $Q = R/L$ is the radius-edge ratio of the tetrahedron with R denoting the radius of the unique circumsphere and L the shortest edge length of the tetrahedron. For all well-shaped tetrahedra, this value is small, and with $Q = \sqrt{6}/4 = 0.612$, the smallest value is achieved for a regular tetrahedron where all edges have the same length. For most badly-shaped tetrahedra, this value is large. The radius-edge ratio can detect almost all degenerated tetrahedra except one type of tetrahedra, which has no small edges, but can have large dihedral angles, so-called slivers. An additional mesh smoothing and optimization step is used to remove the slivers and improve the overall mesh quality. The CDT meshing approach thus produces high-quality tetrahedral meshes, which do not contain any badly shaped tetrahedra. As discussed above, this is an important criterion to ensure good numerical properties of the FEM with CDT meshes.

2.5 Study design

In a first study, the influence of the insulating grids on the simulated potentials is investigated for five radial and tangential dipole sources, which were placed at increasing depths below the grid as shown in Figure 1. The radial dipole direction was defined as the surface normal of the ECoG grid at the ECoG grid electrode, which is closest to the most superficial dipole. Forward simulations were computed in the reference model incorporating the ECoG grids and in the test model ignoring the grids. Potentials on the scalp surface and in the vicinity of the grids inside the volume conductor are visualized to show the influence of the insulating grids. In addition, errors between the simulated

potentials at the EEG and ECoG electrodes in both models were evaluated using the error measures described below.

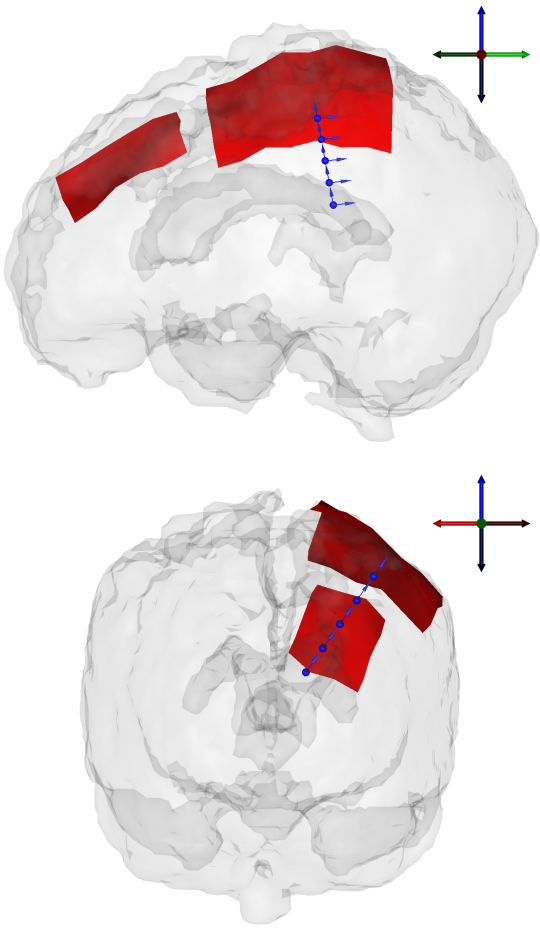

Fig. 1 Side view (top) and rear view (bottom) of the series of 5 radial and tangential dipoles at different depths below the grid.

In a second study, to investigate the influence of the grids on the solution of the inverse problem, sources were distributed across the whole brain volume, with sources placed more densely below the grids. The orientations of the dipole sources were determined to maximize the expected localization errors, when ignoring the influence of the ECoG grids. This was done as follows: For every source, the lead field (dimension $s \times 3$), that is, the potential for a source in x-, y- and z-direction, was computed in the model ignoring the grids and in the model incorporating the grids. Then the singular value decomposition of the difference between these two lead fields was calculated. The right-singular

vector belonging to the largest singular value was chosen as dipole orientation for the forward EEG computations when taking the grid into account. This orientation maximizes the L_2 norm of the potential difference, that is, the relative error, between the solutions ignoring, respectively, incorporating the ECoG grids. For this dipole orientation, which yields the maximum relative error, we expect to find localization errors, which are close to the maximum localization error for any dipole at that position. Plots showing the dipole orientations having maximum relative error are also presented.

Forward simulations were performed in the reference model to generate reference EEG and ECoG data. This data was then reconstructed in the erroneous test model ignoring the insulating electrode sheets using the dipole fitting approach for EEG data, and the goal function scan method for the ECoG data. Differences between the reference dipole sources and the reconstructed dipole sources were evaluated using the error measures described in subsection 2.8. Mislocalization errors for all sources, represented by vectors pointing from the reference to the reconstructed source position, are shown to illustrate the dependence of the localization error on the brain region and to show the mislocalization tendency. In addition average source reconstruction errors are analyzed for sources at different distance intervals to the insulating grids.

2.6 Construction of the reference model

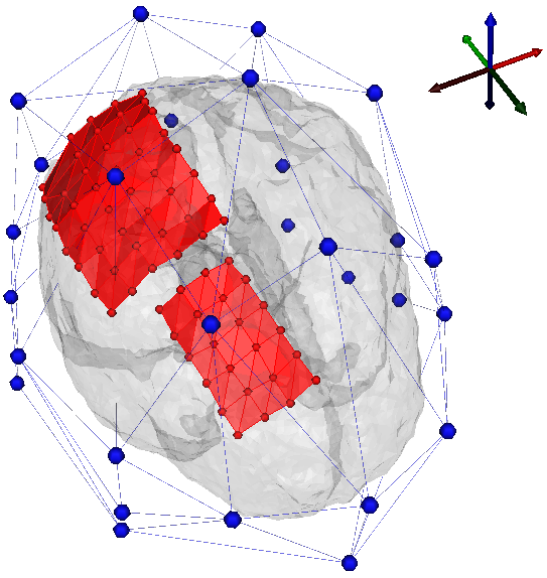

Fig. 2 Surface EEG electrodes (blue) and ECoG electrode grids (red).

To study the influence of the silastic ECoG grids on EEG and ECoG source analysis, a simulation study is carried out in a realistic volume conductor model of a patient, who suffered from medically intractable epilepsy. The patient underwent monitoring with simultaneous intracranial and surface electrodes at the Mayo Clinic, Rochester, USA. Pre-surgically, a T1-weighted MRI was recorded (256 slices in axial, 256 in sagittal and 120 in coronal direction) with a resolution of $0.86 \times 1.6 \times 0.86$ mm. The patient's head was opened and a part of the skull removed for the implantation of two ECoG grids, a 4×6 and a 6×8 electrode grid as shown in Figure 2. For our simulations two grid electrodes were excluded, so that ECoG data was computed at 70 electrodes. The ECoG grids consisted of 0.127 mm thin silastic sheets into which the electrodes were embedded. The removed skull portion was not put back and the remaining skull hole was incorporated into the FEM model. The scalp compartment was then closed, 30 EEG electrodes were placed on the scalp surface as shown in Figure 2 and a pressure bandage was applied. Post-surgically, a Computed Tomography (CT) image was taken (68 slices in axial, 512 in sagittal and 635 in coronal direction) with a resolution of $0.49 \times 0.49 \times 2.65$ mm.

A voxel-based affine registration using mutual information was used to register the pre-surgical T1-MRI onto the post-surgical CT [34]. The registered datasets were then segmented into the four tissue compartments scalp, skull, CSF and brain using an adaptive fuzzy C-means (AFCM) segmentation approach [44]. Scalp, skull and the CSF in the craniotomy opening were extracted from the CT while the remaining part of the CSF-compartment and the brain were segmented out of the T1-MRI.

To model the ECoG grids, the barycenters of the electrodes were extracted from the CT image and triangulated. Duplicates of the two triangulated surfaces were then shifted along the averaged triangle normals by 0.127 mm, that is, the thickness of the grids. By connecting the edges of the original and the shifted grids two closed surfaces were constructed. A CDT was finally applied to build tetrahedra meshes of the volumes of the two ECoG grids. Note, that no simplifications regarding the geometry of the ECoG grids were applied. Triangle meshes of the segmented surfaces scalp, outer skull, inner skull, CSF and brain were obtained from the registered and segmented image datasets using the software CURRY [41]. Due to the craniotomy hole and the brain shift [64] between the pre-surgical MRI and the post-surgical CT, intersections of the resulting triangulated surfaces occurred. Therefore, a first tetrahedralization was obtained using the CDT on the non-intersecting surfaces. Then, one-by-one, the nodes of the CDT meshes of the ECoG grids and the nodes of the triangulated outer and inner skull surfaces were added and new CDT meshes were created. The procedure resulted in a CDT FE mesh with 116,651 nodes and 662,099 elements.

The mean radius-edge ratio across all tetrahedra was 1.29 and only 0.05% of all tetrahedra had a radius-edge ratio larger than 3.0. Even if most Q values are clearly above the optimal value of 0.612, the otherwise limited values still show that we achieved good mesh quality for our special case of a volume conductor with thin silastic grids where a strong adaptive grid refinement is

a more important prerequisite than a completely regular mesh. Thus, a good convergence can be expected for the FEM simulations as deeply discussed in section 2.3.

Finally, a conductivity value was assigned to each tetrahedron by determining which closed segmented surface surrounds the tetrahedron using a solid-angle calculation as described in detail in [49]. Conductivity values of $0.33\,\mathrm{S/m}$, $0.0042\,\mathrm{S/m}$, $1.79\,\mathrm{S/m}$, $0.33\,\mathrm{S/m}$ and $3.3 \times 10^{-11}\,\mathrm{S/m}$ [10,5,77] were used for the compartments scalp, skull, CSF, brain and silastic grids, respectively. For those simulations in which the modeling of the ECoG grids was ignored, a test model was constructed where the conductivity of all grid tetrahedra was set to the value of CSF conductivity. The test model otherwise remained unchanged.

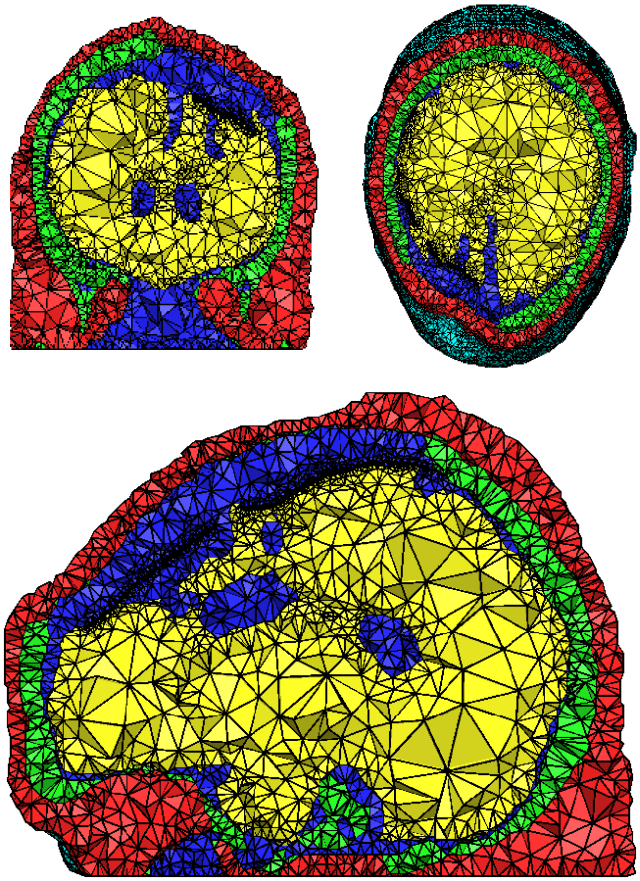

Fig. 3 Coronal (top, left), axial (top, right) and sagittal (bottom) cut views of the tetrahedral FE model of the patient's head with implanted ECoG grids. The compartments are indicated by different colors: Scalp (red), skull (green), CSF (dark blue) and brain (yellow).

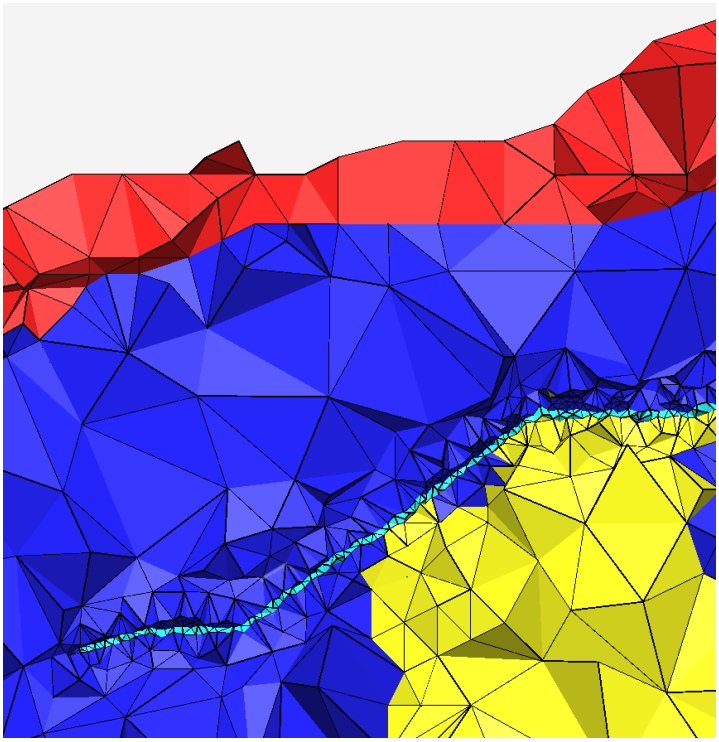

Fig. 4 Close-up view of the area in the FE mesh, where one of the ECoG grids is situated. The compartments are indicated by different colors: Scalp (red), skull (green), CSF (dark blue), brain (yellow) and ECoG grid (light blue).

Cut views of the tetrahedral FE model of the patient's head can be seen in Figure 3, and Figure 4 shows the area in which one of the ECoG grids is situated. It can be observed that in the region around the grids a large number of very fine tetrahedra is needed to describe the geometry of the very thin grids and to guarantee at the same time well-shaped tetrahedra.

2.7 Error measures for forward calculations

To quantify the differences between two solutions to the forward problem, a reference solution $\mathbf{\Phi}^{\mathrm{ref}}$ and a test solution $\mathbf{\Phi}^{\mathrm{test}}$, we use three error measures following [33,35,7,26]: the *relative error* (*RE*), the *relative difference measure* (*RDM*) and the *magnification factor* (*MAG*). The RE can be defined as

$$\mathrm{RE} = \frac{\left\|\mathbf{\Phi}^{\mathrm{ref}} - \mathbf{\Phi}^{\mathrm{test}}\right\|_2}{\left\|\mathbf{\Phi}^{\mathrm{ref}}\right\|_2}, \quad \%\mathrm{RE} = \mathrm{RE} \cdot 100\%, \tag{4}$$

with $\|\cdot\|_2$ being the L_2 norm. The RE is equally affected by changes in topography and in total magnitude of the potentials [35]. Therefore, we introduce

the topography error RDM, and the magnitude error MAG. Following Lew et al. [33] we define the RDM as

$$\mathrm{RDM} = \left\| \frac{\mathbf{\Phi}^{\mathrm{ref}}}{\|\mathbf{\Phi}^{\mathrm{ref}}\|_2} - \frac{\mathbf{\Phi}^{\mathrm{test}}}{\|\mathbf{\Phi}^{\mathrm{test}}\|_2} \right\|_2, \quad \%\mathrm{RDM} = \frac{\mathrm{RDM}}{2} \cdot 100\%, \tag{5}$$

Lew et al. [33] showed that the RDM is related to the cosine of the angle between the vectors $\mathbf{\Phi}_{\mathrm{ref}}$ and $\mathbf{\Phi}_{\mathrm{test}}$, so that the RDM is bounded between 0 and 2. The optimal value of %RDM is therefore 0%, and the maximum value is 100%. The magnitude error MAG is computed as

$$\mathrm{MAG} = \frac{\|\mathbf{\Phi}^{\mathrm{test}}\|_2}{\|\mathbf{\Phi}^{\mathrm{ref}}\|_2}, \quad \%|1 - \mathrm{MAG}| = |1 - \mathrm{MAG}| \cdot 100\%, \tag{6}$$

(optimal value of MAG is 1).

2.8 Error measures for inverse calculations

Analyzing reference data using an ECD estimation procedure results in a reconstructed dipole, which is characterized by its location, its orientation and its magnitude. Errors in the inverse calculations can therefore be quantified by measuring the differences in these dipole parameters. The euclidean distance between the reference dipole position and the position of the reconstructed dipole is used to measure the localization error. As a measure for the orientation error the angle between the reference and the reconstructed dipole orientations is used,

$$\angle(\mathbf{a}; \mathbf{b}) = \arccos \frac{\mathbf{a} \cdot \mathbf{b}}{\|\mathbf{a}\|_2 \cdot \|\mathbf{b}\|_2}. \tag{7}$$

To quantify the error in magnitude, the relative difference between the magnitude of the reference dipole, M_{ref}, and the magnitude of the reconstructed dipole, M_{rec}, is computed,

$$\%\Delta M = \frac{|M_{\mathrm{rec}} - M_{\mathrm{ref}}|}{M_{\mathrm{ref}}} \cdot 100\%. \tag{8}$$

2.9 Software and Computational Platform

CDT meshing was performed using the software TetGen [61]. All source analysis forward and inverse computations were performed within the software toolbox SimBio [63] on a PC equipped with 8 GB of RAM and an *Intel Core 2 Quad Q6600* CPU. Visualization was carried out using the software SCIRun [59].

3 Results

In a first experiment we compared EEG and ECoG forward modeling differences between the models with and without ECoG grids. Table 1 lists the errors in the EEG and ECoG electrode potentials, simulated for the dipoles displayed in Figure 1, caused by not accounting for the ECoG grids in the forward solution. In addition, Figure 5 shows the simulated potentials at the scalp surface (zero-average reference over the head surface) and in the vicinity of the insulating grids inside the volume conductor model for the deepest and the most superficial dipoles. Potentials inside the model are visualized on a plane passing through the positions of the 5 probe dipole sources.

Table 1 Errors between FEM solutions for the scalp EEG and the ECoG incorporating the ECoG grid and ignoring it.

		Scalp EEG		**ECoG**	
Dipole number	**Orientation**	**RDM in %**	**MAG**	**RDM in %**	**MAG**
1 (farthest from the grid)	radial	6.2541	1.0704	19.4246	0.6723
2	radial	8.1315	1.1094	14.9579	0.7025
3	radial	12.8126	1.2165	19.9120	0.5644
4	radial	28.0687	2.0094	17.7442	0.3565
5 (closest to the grid)	radial	37.3872	3.6547	14.2245	0.2817
1	tangential	3.7798	1.0126	9.2548	0.8243
2	tangential	6.7608	1.0372	10.4221	0.7956
3	tangential	13.0755	1.0850	15.8391	0.6782
4	tangential	25.6068	1.2337	23.0515	0.5128
5	tangential	44.7511	1.6391	21.0273	0.3722

No significant difference between the scalp potential distributions can be seen for the deepest dipole while, for more superficial dipoles and especially for the dipole closest to the grid (#5), clear differences can be observed. The RDM and MAG values for the EEG potentials in Table 1 confirm these observations. The RDM is maximal for the most superficial sources #4 and #5, where it reaches values of up to 45%. For the sources close to the grids the MAG is also strongly affected by a screening effect of the grids. Especially for radial sources high MAG values of up to 3.65 are observed, that is, in the model without the grids simulated electrode potentials were up to more than three times as large as compared to the model incorporating the grids.

Although the potentials inside of the volume conductor in the region close to the source do not seem to differ for the deepest sources, it is evident from the iso-potential lines that the potentials do differ in the vicinity of the insulating grids. It can be observed that the iso-potential lines in the model with ECoG grids are denser below the grid and less dense in the area between the grid and the scalp surface. Iso-potential lines were plotted at the same iso-values in the models with and without grids. Thus, this indicates that the ECoG

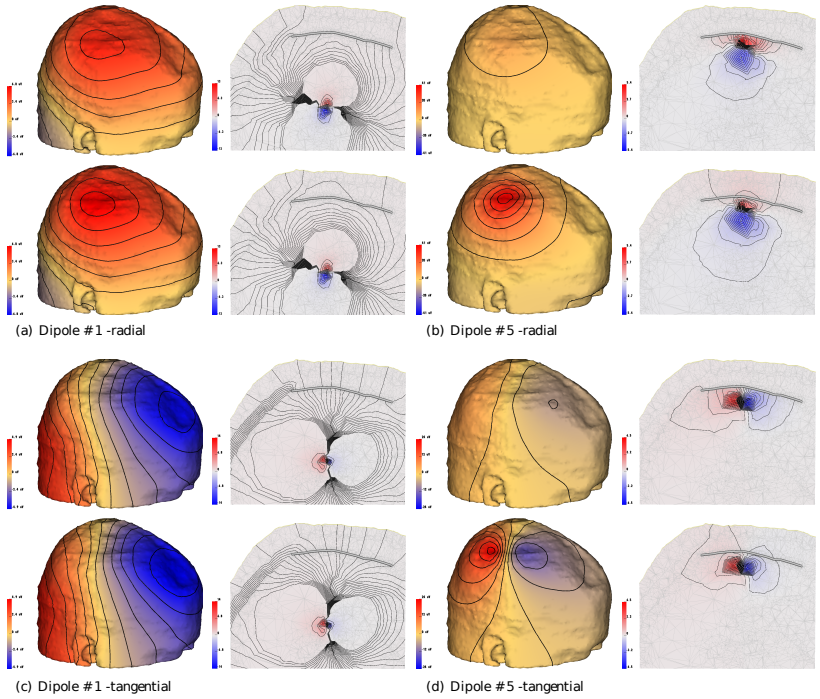

Fig. 5 Potentials on the scalp surface and in the volume below the grids for the deepest (dipole #1, (a, c)) and most superficial (dipole #5, (b, d)) dipoles for radial (a, b) and tangential (c, d) dipole orientations. Upper row: FEM potentials with ECoG grid. Lower row: FEM potentials without ECoG grid. Potential scales for upper and lower rows are identical. Zero-average reference over the outer model surface was used for the potentials on the scalp surface. Equidistant iso-potential lines are plotted on the scalp surface and in the volume. Additional equidistant iso-potential lines are shown in a and c to better illustrate the potential differences in the vicinity of the insulating ECoG grids.

potentials are smaller when ignoring the grid as compared to when modeling the grid. The MAG values (< 0.4) for the ECoG potentials of dipole #1 in Table 1 confirm this observation. It is notable that even for the most distant dipole position the RDM values for the ECoG data - ranging between 9% and 20% - are large, and even larger than the RDM values for the scalp EEG data. The influence of the insulating grids on the potentials in the vicinity of the grid is even more obvious for the most superficial radial and tangential dipoles as shown in Figures 5b and d. When ignoring the insulating grids the iso-potential lines can pass through the area of the grids unhindered. In contrast, when incorporating the grids the iso-potential lines are compressed below the grid and the potential distribution is distorted. This is also clearly visible in the ECoG RDM values presented in Table 1.

Figure 6 displays the dipole orientations, for which the simulated scalp EEG is maximally influenced by the ECoG grids, as measured by the relative

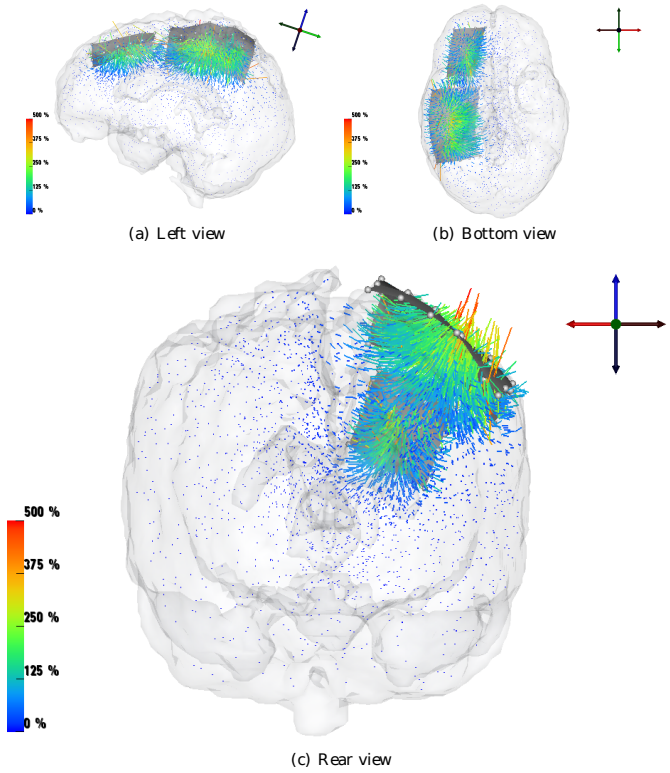

Fig. 6 For each dipole position, a line is shown indicating the dipole orientation that causes maximal RE between the EEG forward solutions incorporating, respectively, ignoring the ECoG grids. The lines are scaled with the RE values.

error between the models incorporating and ignoring the insulating grids. It can be observed, that for positions directly beneath the center of one of the grids, dipoles with an orientation perpendicular to the grid are maximally affected. Towards the edges of the ECoG grids the dipole orientations with maximum relative error become more and more tangential to the grid. In addition, from the length of the lines displayed in Figure 6, it can be seen that the RE is maximal for sources closely beneath the grids and below the center of one of the grids.

In the next study, effects of the ECoG grids on the EEG and ECoG inverse solutions were investigated. For each of the sources, that were distributed across the whole brain volume, with the orientations causing the maximal influence (as described in Section 2.5) a reference solution was generated by simulating the potential at the EEG and ECoG electrodes in the reference volume conductor model incorporating the ECoG grids. ECD estimation (moving dipole fitting for the EEG [56,39] and goal function scan for the ECoG [39,24]) was then performed to reconstruct these reference data. The forward solutions for the ECD estimation were calculated in the model ignoring the ECoG grids.

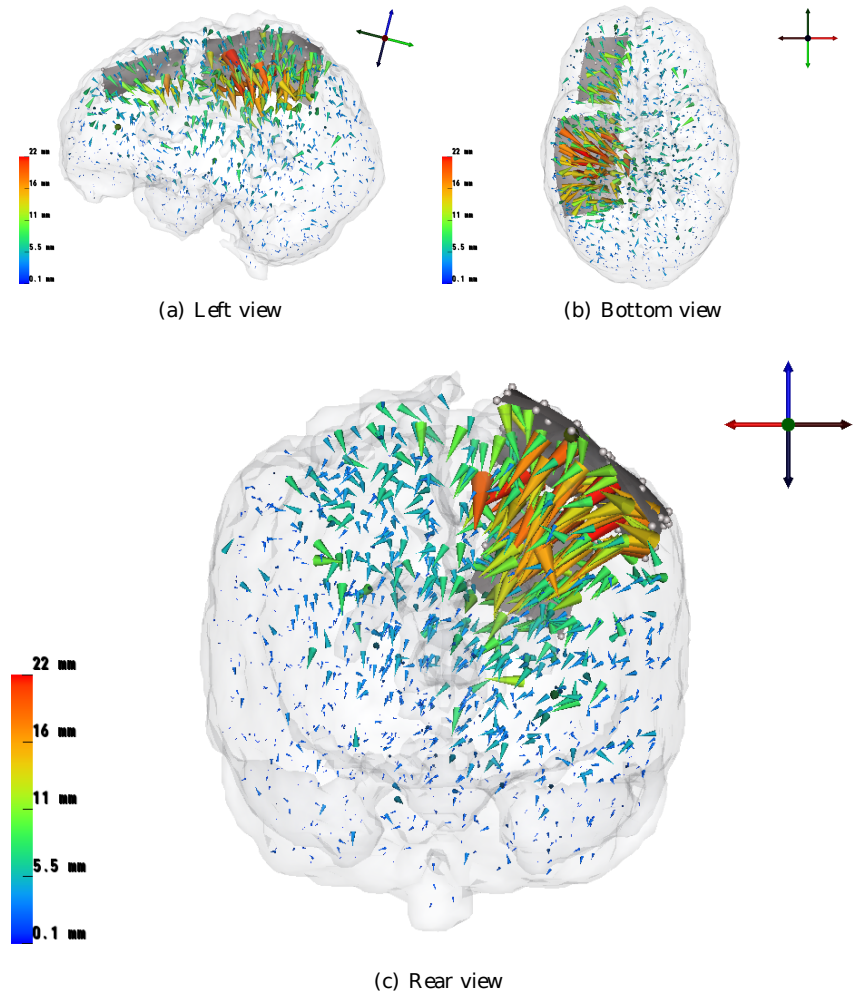

Fig. 7 Localization errors from scalp EEG data when ignoring the insulating ECoG grids. A 10 mm regular grid was superimposed on the complete source space, and mislocalizations for all sources in the same cell of the grid were averaged, to improve the clarity of the visualization. The plotted vectors are pointing from the reference to the reconstructed source position.

Figures 7 and 8 show the resulting mislocalizations. In addition, Table 2 lists the average localization, orientation and magnitude errors across sources at four different distance intervals from the ECoG grids. We will first describe the source reconstruction errors from the scalp EEG reference data. It can be seen from Figure 7 and Table 2 that for sources lying in the distance range up to 1 cm from the grids large errors of 1 cm to more than 2 cm (average of 1.34 cm) in localization occurred when reconstructing the scalp EEG reference data. For these sources errors in orientation were on average 42.2° and the

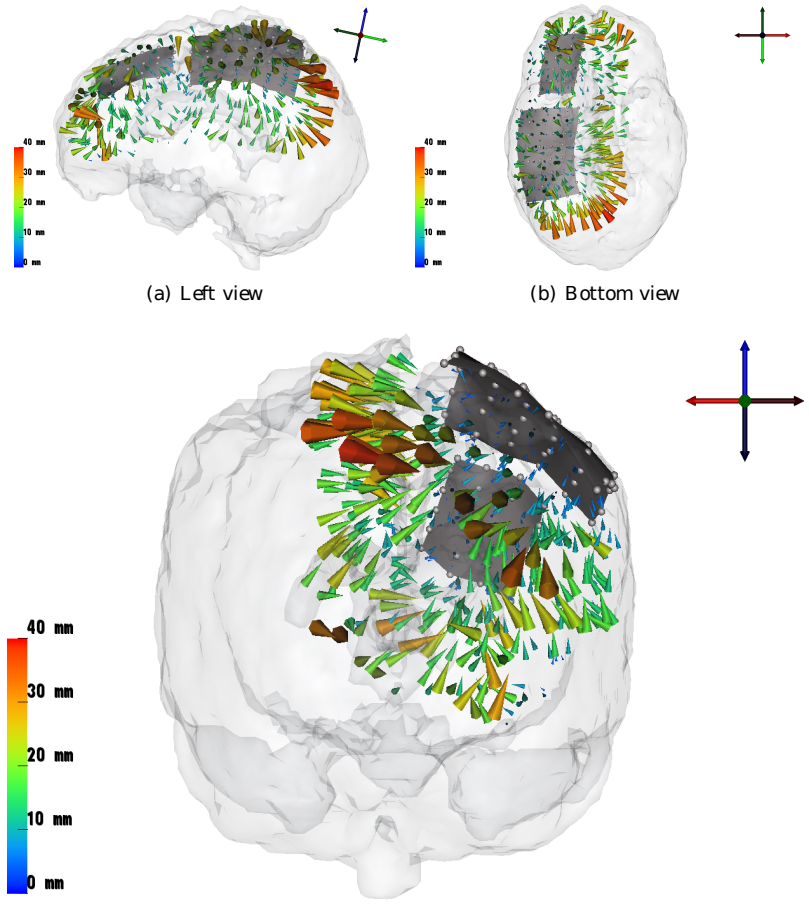

Fig. 8 Localization errors from ECoG data when ignoring the insulating ECoG grids. A 10 mm regular grid was superimposed on the complete source space, and mislocalizations for all sources in the same cell of the grid were averaged, to improve the clarity of the visualization. The plotted vectors are pointing from the reference to the reconstructed source position and vectors were scaled by a factor of 0.5. In addition, only sources at a maximum distance of 40 mm from the ECoG grids were included in this figure.

mean magnitude error was 211.2 %. The arrows in Figure 7 indicate that the sources tended to be reconstructed deeper in the brain, that is, away from the grids. In addition it can be observed, that sources lying close to the edges of the grids were reconstructed deeper and at positions lying more below the center of one of the grids. The reconstruction of sources which were positioned at a distance larger than 4 cm to the grids was not much affected with an average localization error of 2.7 mm, an average orientation error of 2.9° and an average magnitude error of 5 %. This is especially true for sources contralateral to the grids.

Table 2 Average errors of the ECD estimation results from scalp EEG and ECoG reference data across four different distance ranges from the ECoG grids. The magnitude error $\%\Delta M$ is defined in Equation (8).

	Scalp EEG			**ECoG**		
Distance ∅ in mm	**Localization** ∅ in mm	**Orientation** ∅ in ˚	$\%\Delta M$ ∅ in %	**Localization** ∅ in mm	**Orientation** ∅ in ˚	$\%\Delta M$ ∅ in %
$d <= 10$	13.4	42.2	211.2	5.4	77.5	686.4
$10 < d <= 20$	12.4	20.1	35.7	8.9	51.0	84.5
$20 < d <= 40$	7.1	7.6	18.3	17.2	53.6	52.6
$d >= 40$	2.7	2.9	5.0	26.5	87.6	339.2

Errors for the source reconstruction based on the ECoG reference data are presented in Figure 8 and in Table 2. With regard to the localization error sources closer than 1 cm to the grid are least affected with an average error of 5.4 mm. The localization error strongly increases for more distant sources, most likely due to the limited field-of-view of the ECoG. Already in the distance range from 2 to 4 cm the average localization error rises to 17.2 mm. From Figure 8 we observe that sources tend to be reconstructed at positions more towards the insulating ECoG grids. For sources close to the border of the ECoG grids, for example, we can observe that they are by tendency reconstructed at positions more towards the center of the closest grid. With respect to the orientation and magnitude of the reconstructed sources large errors of on average 77.5˚, respectively, 686.6% can be found even for the sources immediately below the grid. Orientation and magnitude errors stay on a high level ranging between 51.0˚and 87.6˚, respectively, 52.6% and 339.2% for more distant sources.

4 Discussion

In our results we observed a tendency of sources close to the border of the grids to be localized at positions towards the grid's center during EEG source reconstruction when not accounting for the insulating ECoG grids. As already pointed out in the introduction simultaneously measured EEG data can be analyzed in practice to verify the correct placement of the ECoG grid. The observed mislocalization tendency can have consequences for this application. In the case of an epileptic source close to the border of the ECoG grid, the evaluation of the scalp EEG without taking the insulating ECoG grids into account would indicate, due to the mislocalization tendency, that the source is lying well below the grid. Thus, the suboptimal placement of the ECoG grid would not be detected. Only when incorporating the insulating grids in the volume conductor model it would be possible to recognize that the grid is not placed above the epileptic source and the grid placement could be corrected.

For ECoG source reconstruction it was found that sources immediately below the grids were less affected with regard to their localization error (on aver-

age 5.4 mm at distances up to 1 cm from the grids), but their moments could only be reconstructed with big errors of, on average, 77.5° in orientation and 686.4% in magnitude. In [53,42] it was reported that ECD orientations might even be more important than absolute localizations in attributing epileptic activity to subcompartments of the respective brain area. We therefore conclude that also for ECoG source analysis, an accurate modeling of the insulating ECoG grids might be important.

In our reference model the ECoG grids were located on the right superior frontal and parietal cortex. As the presented results are in general very clear, we do not expect significantly different outcomes when considering insulating grids placed on other cortex regions. There might, however, be some cases were the influence of the grids on the scalp EEG might be smaller. From the potential distributions inside the model (Figure 5) we learned that the presence of the grid mainly affects the potentials in the vicinity of the grid. When the grid is placed on the inferior temporal lobe, for example, then there might be only few or no electrodes on the scalp surface close to the grid. Thus, the scalp EEG would be less affected. The influence on the ECoG data, however, should still be very similar to the results presented here.

A comparable study to the one presented here was performed by Zhang et al. [77]. However, their study focused on investigating the effect of insulating ECoG grids on the cortical potential imaging (CPI) method, so that we cannot compare our source reconstruction results obtained using ECD estimation to theirs. In particular, Zhang et al. express the influence of the grids on the results of their CPI approach in terms of correlation between the directly simulated and the reconstructed cortical potentials. We, however, are able to make statements regarding the actual localization errors in mm that are to be expected when ignoring the insulating grids. Nevertheless, we can compare our results regarding the influence of the grids on the scalp potential maps to the results in Zhang et al.'s study. The authors report, that the scalp potential magnitude simulated in the model incorporating the insulating electrode grid strongly decreases, especially for radial dipoles, pointing towards the grid. This is in good agreement with the results presented in Figure 5. Furthermore, Zhang et al. find decreasing values of the correlation coefficient (CC) between the scalp potentials simulated with and without ECoG grids, when the dipole source approaches the grid. The RDM is related to the CC through $\mathrm{RDM} = \sqrt{2(1-\mathrm{CC})}$ [76]. Therefore, the decreasing CC found by Zhang et al. is in agreement with the increasing RDM in our study, that is, an increased topography error, for sources approaching the grids. Our findings with regard to the influence of the insulating grids on the ECoG data are new and have not yet been reported in the literature. We believe that these results are important and of interest for many researchers working on ECoG based source analysis.

The findings presented in this article might also aid in the interpretation of previous work related to the simultaneous measurement of ECoG and scalp EEG. In [67,66], for example, the cerebral EEG substrates of scalp EEG seizure patterns were determined to assess the limitations of scalp seizure recording in

the localization of seizure onset zones in patients with temporal lobe epilepsy. In light of our results, it is an interesting question whether the silastic membrane of the subdural grids may have attenuated the scalp EEG. This could have given a bias to the interpretation that a synchronously-active cortical area of minimally $10\,\mathrm{cm}^2$ is required to generate a scalp recognizable interictal spike or ictal rhythm and that a percentage of spikes lacked sufficient synchrony to result in a clearly localized or lateralized scalp ictal pattern [67, 66].

Although we took care to construct a detailed and realistic volume conductor model for our simulation study, some limitations of the model must be discussed. Due to the brain shift, which occurs when the skull of the patient is opened during surgery, the alignment of the pre-surgical MRI and the post-surgical CT was suboptimal. Therefore, we have to expect some inaccuracy in the segmentation of the CSF and the brain compartments in the area of the craniotomy hole. It shall first be noted, that, even if a post-surgical MRI was not available to us, to the best of our knowledge, there should be generally no technical obstacles for measuring an MRI after the surgery. This post-surgical MRI should then in practice be used for model construction. Another, however more difficult, solution strategy could be the modeling of the brain shift as reported by Soza [64] and its subsequent use for an improved registration of a pre-surgical MRI and a post-surgical CT. A further important aspect to be discussed here are the chosen conductivity values for the different tissue compartments. In our investigations standard isotropic conductivity values were used for all segmented tissue compartments [10, 5, 77]. However, as recent studies have shown, the skull might be better represented by a model that distinguishes compact and cancellous bone tissue [30, 1, 12] and the brain is known to have an inhomogeneous and anisotropic conductivity [18, 72, 52, 16]. Furthermore, conductivity parameters are known to vary inter- and intra-individually [30, 1, 32]. However, as those errors affect the reference and the test model alike we do not assume that an improved modeling with regard to those aspects would have had a significant influence on the results presented here.

In Sections 2.3 and 2.4, based on our experience, we manually determined the important parameters for the setup of optimal FE forward solutions for all sources in our sophisticated volume conductor scenario. We would like to note that optimized numerical accuracy can in some applications also be achieved by using automatically adapted finite element refinement strategies (see, e.g., [79], chapter 14). One of our future goals is to investigate how such automatic adaptation algorithms can contribute to FE-based source analysis.

In the present study we employed a CDT, instead of a hexahedral meshing approach for FE model creation. A hexahedral meshing approach could not be used for this epilepsy patient's head model incorporating the thin ECoG grids without also employing advanced techniques, like local refinement and treatment of 'hanging' or 'irregular nodes' [57]. Nevertheless, we would like to mention that hexahedral FE approaches [76, 72, 57, 73, 52, 68] are very at-

tractive for source analysis in standard volume conductor models, especially because no explicit description of the compartment boundaries is required.

Another important tool for epilepsy diagnosis is the simultaneous measurement of MEG and ECoG [38]. One of the great advantages of MEG is that it is much less affected by volume conduction effects than EEG [19,74]. We assume that this should also be true for MEG recordings in the presence of the implanted insulating ECoG grids. Thus, for non-radial sources, reconstruction errors should be mostly negligible when not modeling the grids for MEG source analysis. Nevertheless, for sources very close to the insulating grids, the volume currents in the vicinity of the source, that are also contributing to the MEG signal, should be considerably distorted and, as a consequence, the MEG might also be influenced by the silastic ECoG grids. Further investigations are necessary to quantify this influence.

In conclusion, our study has shown that the insulating ECoG grids strongly distort the potential distribution in the vicinity of the grids. This resulted in large errors for the simultaneously measured surface EEG, especially for sources lying beneath the grid, and to significant errors for the source reconstruction from scalp EEG data. The ECoG data was also shown to be strongly affected by the insulating properties of the electrode sheet, and considerable source reconstruction errors were found even for sources immediately below the grid.

For the first time, source reconstruction errors employing widely-used ECD estimation approaches and evaluating probe sources distributed throughout the whole brain volume were presented and analyzed. The presented mislocalization maps can help interpreting EEG and ECoG source reconstruction results where the insulating ECoG grids were ignored. Furthermore, an alternative way was described of generating suitable volume conductor models with good convergence properties for solving the forward problem taking into account the very thin insulating ECoG grids. From the observed forward and inverse errors, we conclude, that the highly insulating silastic ECoG grids have to be taken into account for the analysis of scalp EEG data measured in the presence of the insulating ECoG grids. In addition, it might also be beneficial to account for the insulating grids when analyzing ECoG data. In practice, the insulating grids could be taken into account using the finite element method based on adapted, high-quality CDT finite element meshes and using freely-available software, as it was described in this work.

Acknowledgment

This work was supported by the Deutsche Forschungsgemeinschaft (WO1425/2-1, STE380/14-1). The authors would like to thank Chris Johnson, Tolga Tasdizen and Darby J. Van Uitert from the SCI Institute, University of Utah, Salt Lake City, USA, Gregory A. Worrell from the Department of Neurology and Division of Epilepsy, Mayo Clinic, Rochester, Minnesota, USA, and Scott Makeig from the Swartz Center for Computational Neuroscience, University

of California San Diego, USA, for providing the necessary data for model construction and for their valuable help and the fruitful discussions with regard to this study. We would also like to thank the anonymous reviewers for their helpful critics and comments that significantly improved our manuscript.

References

1. Akhtari, M., Bryant, H., Mamelak, A., Flynn, E., Heller, L., Shih, J., Mandelkem, M., Matlachov, A., Ranken, D., Best, E., et al.: Conductivities of three-layer live human skull. Brain Topography **14**(3), 151–167 (2002)
2. Alarcon, G., Kissani, N., Dad, M., Elwes, R., Ekanayake, J., Hennessy, M., Koutroumanidis, M., Binnie, C., Polkey, C.: Lateralizing and localizing values of ictal onset recorded on the scalp: Evidence from simultaneous recordings with intracranial foramen ovale electrodes. Epilepsia **42**(11), 1426–1437 (2001)
3. Bast, T., Boppel, T., Rupp, A., Harting, I., Hoechstetter, K., Fauser, S., Schulze-Bonhage, A., Rating, D., Scherg, M.: Noninvasive source localization of interictal EEG spikes: effects of signal-to-noise ratio and averaging. J.Clin.Neurophysiol. **23**(6), 487–497 (2006)
4. Bast, T., Oezkan, O., Rona, S., Stippich, C., Seitz, A., Rupp, A., Fauser, S., Zentner, J., Rating, D., Scherg, M.: EEG and MEG source analysis of single and averaged interictal spikes reveals intrinsic epileptogenicity in focal cortical dysplasia. Epilepsia **45**(6), 621–631 (2004)
5. Baumann, S., Wozny, D., Kelly, S., Meno, F.: The electrical conductivity of human cerebrospinal fluid at body temperature. IEEE Trans Biomed Eng **44**(3), 220–223 (1997)
6. Baumgartner, C., Lindinger, G., Ebner, A., Aull, S., Serles, W., Olbrich, A., Lurger, S., Czech, T., Burgess, R., Luders, H.: Propagation of interictal epileptic activity in temporal lobe epilepsy. Neurology **45**(1), 118–122 (1995)
7. Bertrand, O., Thévenet, M., Perrin, F.: 3D finite element method in brain electrical activity studies. In: J. Nenonen, H. Rajala, T. Katila (eds.) Biomagnetic Localization and 3D Modelling, pp. 154–171. Report of the Dep. of Tech.Physics, Helsinki University of Technology (1991)
8. Braess, D.: Finite Elements: Theory, Fast Solvers and Applications in Solid Mechanics. Cambridge University Press (2007)
9. van den Broek, S., Reinders, F., Donderwinkel, M., Peters, M.: Volume conduction effects in EEG and MEG. Electroenc. Clin. Neurophysiol. **106**, 522–534 (1998)
10. Buchner, H., Knoll, G., Fuchs, M., Rienäcker, A., Beckmann, R., Wagner, M., Silny, J., Pesch, J.: Inverse localization of electric dipole current sources in finite element models of the human head. Electroenc. Clin. Neurophysiol. **102**, 267–278 (1997)
11. Cook, M., Koles, Z.: A high-resolution anisotropic finite-volume head model for EEG source analysis. In: Proc. of the 28th Annual Int. Conf. of the IEEE Engineering in Medicine and Biology Society, pp. 4536–4539 (2006)
12. Dannhauer, M., Lanfer, B., Wolters, C., Knösche, T.: Modeling of the human skull in EEG source analysis. Human Brain Mapping **32**(9), 1383–1399 (2011). DOI: 10.1002/hbm.21114, PMID: 20690140
13. Dümpelmann, M., Fell, J., Wellmer, J., Urbach, H., Elger, C.: 3D source localization derived from subdural strip and grid electrodes: A simulation study. Clin.Neurophysiol. **120**, 1061–1069 (2009)
14. Ebersole, J.: Non-invasive pre-surgical evaluation with EEG/MEG source analysis. Electroenc.Clin.Neurophysiol.Suppl. **50**, 167–174 (1999)
15. Fuchs, M., Wagner, M., Kastner, J.: Development of volume conductor and source models to localize epileptic foci. Journal of Clinical Neurophysiology **24**(2), 101–119 (2007). DOI 10.1097/WNP.0b013e318038fb3e
16. Güllmar, D., Haueisen, J., Reichenbach, J.: Influence of anisotropic electrical conductivity in white matter tissue on the EEG/MEG forward and inverse solution. a high-resolution whole head simulation study. NeuroImage (2010). Doi:10.1016/j.neuroimage.2010.02.014

17. Hackbusch, W.: Elliptic differential equations. Springer (1992)
18. Hallez, H., Vanrumste, B., Hese, P.V., D'Asseler, Y., Lemahieu, I., de Walle, R.V.: A finite difference method with reciprocity used to incorporate anisotropy in electroencephalogram dipole source localization. Phys.Med.Biol. **50**, 3787–3806 (2005)
19. Hämäläinen, M., Hari, R., R.Ilmoniemi, Knuutila, J., O.Lounasmaa: Magnetoencephalography: theory, instrumentation, and applications to noninvasive studies of the working human brain. Rev.Mod.Phys. **65**, 413–497 (1993)
20. Hämäläinen, M., Ilmoniemi, R.: Interpreting magnetic fields of the brain: minimum norm estimates. Med & Biol Eng & Comp **32**, 35–42 (1994)
21. Huiskamp, G., Maintz, J., Wieneke, G., Viergever, M., van Huffelen, A.: The influence of the use of realistic head geometry in the dipole localization of interictal spike activity in MTLE patients. Biomedizinische Technik **42**, 84–87 (1997)
22. Huiskamp, G., Oostendorp, T., Hoekema, R., Leijten, F.: Simultaneous eeg/meg and ecog source characterization of interictal spikes. In: BIOMAG2000, Proc. of the 12th Int. Conf. on Biomagnetism (2000). URL http://biomag2000.hut.fi
23. Huiskamp, G., Vroeijenstijn, M., van Dijk, R., Wieneke, G., van Huffelen, A.: The need for correct realistic geometry in the inverse EEG problem. IEEE Trans Biomed Eng **46**(11), 1281–1287 (1999)
24. Knösche, T.: Solutions of the neuroelectromagnetic inverse problem. Ph.D. thesis, University of Twente, The Netherlands (1997)
25. Kobayashi, K., Merlet, I., Gotman, J.: Separation of spikes from background by independent component analysis with dipole modeling and comparison to intracranial recordings. Clin. Neurophysiol. **112**(3), 405–413 (2001)
26. Kybic, J., Clerc, M., Abboud, T., Faugeras, O., Keriven, R., Papadopoulo, T.: A common formalism for the integral formulations of the forward EEG problem. IEEE Trans. Med. Imag. **24**(1), 12–18 (2005)
27. Lai, Y., van Drongelen, W., Ding, L., Hecox, K., Towle, V., Frim, D., He, B.: Estimation of in vivo human brain-to-skull conductivity ratio from simultaneous extra- and intracranial electrical potential recordings. Clin.Neurophysiol. **116**, 456–465 (2005)
28. Lantz, G., Holub, H., Ryding, E., Rosen, I.: Simultaneous intracranial and extracranial recordings of interictal epileptiform activity in patients with drug resistent partial epilepsy: patterns of conduction and results from dipole reconstructions. Electroenc.Clin.Neurophysiol. **99**, 69–78 (1996)
29. Lantz, G., de Peralta, M.G., Gonzalez, A., Michel, C.: Noninvasive localization of electromagnetic epileptic activity. II. Demonstration of sublobar accuracy in patients with simultaneous surface and depth recordings. Brain Topography **14**(2), 139–147 (2001)
30. Law, S.: Thickness and resistivity variations over the upper surface of the human skull. Brain Topography **6**(2), 99–109 (1993)
31. Leeman, B., Cole, A.: Advancements in the treatment of epilepsy. Annual Review of Medicine **59**(1), 503–523 (2008). DOI 10.1146/annurev.med.58.071105.110848. URL http://arjournals.annualreviews.org/doi/abs/10.1146/annurev.med.58.071105.110848
32. Lew, S., Wolters, C., Anwander, A., Makeig, S., MacLeod, R.: Improved eeg source analysis using low resolution conductivity estimation in a four-compartment finite element head model. Human Brain Mapping **30**(9), 2862–2878 (2009). Http://dx.doi.org/10.1002/hbm.20714, NIHMSID: 95584, PMID: 19117275, PMCID: PMC2733918
33. Lew, S., Wolters, C., Dierkes, T., Röer, C., MacLeod, R.: Accuracy and run-time comparison for different potential approaches and iterative solvers in finite element method based EEG source analysis. Applied Numerical Mathematics **59**(8), 1970–1988 (2009). DOI DOI: 10.1016/j.apnum.2009.02.006. URL http://www.sciencedirect.com/science/article/pii/S016892740900021X. NIHMSID 120338, PMCID: PMC2791331
34. Maes, F., Vandermeulen, D., Marchal, G., Suetens, P.: Multimodality image registration by maximization of mutual information. IEEE Trans Med Imag **16**(2), 187–198 (1997)
35. Meijs, J., Weier, O., Peters, M., van Oosterom, A.: On the numerical accuracy of the boundary element method. IEEE transactions on biomedical engineering **36**(10), 1038–1049 (1989)
36. Merlet, I., Gotman, J.: Reliability of dipole models of epileptic spikes. Clinical Neurophysiol. **110**(6), 1013–1028 (1999)

37. Michel, C., Murray, M., G.Lantz, S.Gonzalez, L.Spinelli, de Peralta, R.: EEG source imaging. Clin.Neurophysiol. **115**, 2195–2222 (2004). Invited review
38. Mikuni, N., Nagamine, T., Ikeda, A., Terada, K., Taki, W., Kimura, J., Kikuchi, H., Shibasaki, H.: Simultaneous recording of epileptiform discharges by MEG and subdural electrodes in temporal lobe epilepsy. NeuroImage **5**(4), 298–306 (1997). DOI 10.1006/nimg.1997.0272. URL http://www.sciencedirect.com/science/article/pii/S105381199790272X
39. Mosher, J., Lewis, P., Leahy, R.: Multiple dipole modeling and localization from spatio-temporal MEG data. IEEE Trans Biomed Eng **39**(6), 541–557 (1992)
40. de Munck, J., Peters, M.: A fast method to compute the potential in the multisphere model. IEEE Trans Biomed Eng **40**(11), 1166–74 (1993)
41. Neuroscan: CURRY (2009). CURrent Reconstruction and Imaging
42. Pataraia, E., Lindinger, G., Deecke, L., Mayer, D., Baumgartner, C.: Combined MEG/EEG analysis of the interictal spike complex in mesial temporal lobe epilepsy. NeuroImage **24**, 607–14 (2005)
43. Penfield, W.: The surgical therapy of temporal lobe seizures. Trans.Am.Neurol.Assoc. **51**, 146–149 (1950)
44. Pham, D., Prince, J.: An adaptive fuzzy C-means algorithm for image segmentation in the presence of intensity inhomogeneities. Pat. Rec. Let. **20**, 57–68 (1998)
45. Plummer, C., Harvey, A., Cook, M.: EEG source localization in focal epilepsy: where are we now? Epilepsia **49**(2), 201–218 (2008)
46. Pursiainen, S., Sorrentino, A., Campi, C., Piana, M.: Forward simulation and inverse dipole localization with the lowest order raviart-thomas elements for electroencephalography. Inverse Problems **27**(4) (2011). DOI 10.1088/0266-5611/27/4/045003
47. Ramon, C., Schimpf, P., Haueisen, J., Holmes, M., Ishimaru, A.: Role of soft bone, csf and gray matter in EEG simulations. Brain Topography **16**(4), 245–248 (2004)
48. Ray, A., Tao, J., Hawes-Ebersole, S., Ebersole, J.: Localizing value of scalp EEG spikes: a simultaneous scalp and intracranial study. J.Clin.Neurophysiol. **118**(1), 69–79 (2007)
49. Röer, C.: Source analysis of simultaneous eeg and ecog mesurements in presurgical epilepsy diagnosis. Diplomarbeit in physik, Institut für Biomagnetismus und Biosignalanalyse, Universitätsklinikum Münster (2008)
50. Rosenow, F., Luders, H.: Presurgical evaluation of epilepsy. Brain **124 (Pt 9)**, 1683–1700 (2001)
51. Roth, B., Ko, D., von Albertini-Carletti, I., Scaffidi, D., Sato, S.: Dipole localization in patients with epilepsy using the realistically shaped head model. Electroenc. Clin. Neurophysiol. **102**, 159–166 (1997)
52. Rullmann, M., Anwander, A., Dannhauer, M., Warfield, S., Duffy, F., Wolters, C.: EEG source analysis of epileptiform activity using a 1mm anisotropic hexahedra finite element head model. NeuroImage **44**(2), 399–410 (2009). Http://dx.doi.org/10.1016/j.neuroimage.2008.09.009, PMID: 18848896, NIHMS: 83340, PMCID: PMC2642992, http://www.ncbi.nlm.nih.gov/pmc/articles/PMC2642992/
53. Salayev, K., Nakasato, N., Ishitobi, M., Shamoto, H., Kanno, A., Iinuma, K.: Spike orientation may predict epileptogenic side across cerebral sulci containing the estimated equivalent dipole. Clin. Neurophysiol. **117**, 1836–43 (2006)
54. Sarvas, J.: Basic mathematical and electromagnetic concepts of the biomagnetic inverse problem. Phys.Med.Biol. **32**(1), 11–22 (1987)
55. Scherg, M., Bast, T., Berg, P.: Multiple source analysis of interictal spikes: goals, requirements, and clinical value. J.Clin.Neurophysiol. **16**(3), 214–224 (1999)
56. Scherg, M., Von Cramon, D.: Evoked dipole source potentials of the human auditory cortex. Electroencephalogr Clin Neurophysiol **65**(5), 344–60 (1986)
57. Schimpf, P., Haynor, D., Kim, Y.: Object-free adaptive meshing in highly heterogeneous 3-D domains. International Journal of Bio-Medical Computing **40**(3), 209–225 (1996). DOI 10.1016/0020-7101(95)01146-3. URL http://www.sciencedirect.com/science/article/pii/0020710195011463
58. Schwarz, H.: Methode der finiten Elemente. B.G.Teubner Stuttgart (1991)
59. Scientific Computing and Imaging Institute (SCI): SCIRun: A scientific computing problem solving environment. URL http://www.scirun.org

60. Si, H.: Adaptive tetrahedral mesh generation by constrained Delaunay refinement. International Journal for Numerical Methods in Engineering **75**(7), 856–880 (2008). DOI 10.1002/nme.2318. URL http://dx.doi.org/10.1002/nme.2318
61. Si, H.: TetGen – a quality tetrahedral mesh generator and three-dimensional delaunay triangulator, user's manual. Tech. rep., Weierstraß-Institut für Angewandte Analysis und Stochastik, Berlin (2009). Http://tetgen.berlios.de
62. Si, H., Gärtner, K.: Meshing piecewise linear complexes by constrained Delaunay tetrahedralizations. In: Proc. 14th International Meshing Roundtable, pp. 147–163. Sandia National Laboratories (2005)
63. SimBio Development Group: SimBio: A generic environment for bio-numerical simulations. online, https://www.mrt.uni-jena.de/simbio, accessed June 15 (2012)
64. Soza, G.: Registration and simulation for the analysis of intraoperative brain shift. Ph.D. thesis, Faculty of Computer Science, Friedrich-Alexander-Universität Erlangen-Nürnberg (2005)
65. Stefan, H., Hummel, C., Scheler, G., Genow, A., Druschky, K., Tilz, C., Kaltenhauser, M., Hopfengartner, R., Buchfelder M. andRomstock, J.: Magnetic brain source imaging of focal epileptic activity: a synopsis of 455 cases. Brain **126**(Pt 11), 2396–2405 (2003)
66. Tao, J., Baldwin, M., Hawes-Ebersole, S., Ebersole, J.: Cortical substrates of scalp EEG epileptiform discharges. J.Clin.Neurophysiol. **24**(2), 96–100 (2007)
67. Tao, J., Baldwin, M., Ray, A., Hawes-Ebersole, S., Ebersole, J.: The impact of cerebral source area and synchrony on recording scalp electroencephalography ictal patterns. Epilepsia **48**(11), 2167–2176 (2007)
68. Vallaghe, S., Papadopoulo, T.: A trilinear immersed finite element method for solving the electroencephalography forward problem. SIAM Journal on Scientific Computing **32**(4), 2379 (2010). DOI 10.1137/09075038X
69. Waberski, T., Gobbele, R., Herrendorf, G., Steinhoff, B., Kolle, R., Fuchs, M., Paulus, W., Buchner, H.: Source reconstruction of mesial-temporal epileptiform activity: Comparison of inverse techniques. Epilepsia **41**(12), 1574–583 (2000)
70. Weinstein, D., Zhukov, L., Johnson, C.: Lead-field bases for electroencephalography source imaging. Annals of Biomed.Eng. **28**(9), 1059–1066 (2000)
71. Wiebe, S., Blume, W., Girvin, J., Eliasziw, M.: A randomized, controlled trial of surgery for temporal-lobe epilepsy. The New England Journal of Medicine **345**(5), 311–318 (2001)
72. Wolters, C.: Finite element method based electro- and magnetoencephalography source analysis in the human brain. Habilitation in mathematics, Faculty of Mathematics and Natural Sciences, University of Münster, Germany (2008)
73. Wolters, C., Anwander, A., Berti, G., Hartmann, U.: Geometry-adapted hexahedral meshes improve accuracy of finite element method based EEG source analysis. IEEE Trans.Biomed.Eng. **54**(8), 1446–1453 (2007). DOI http://dx.doi.org/10.1109/TBME.2007.890736
74. Wolters, C., Anwander, A., Weinstein, D., Koch, M., Tricoche, X., MacLeod, R.: Influence of tissue conductivity anisotropy on EEG/MEG field and return current computation in a realistic head model: A simulation and visualization study using high-resolution finite element modeling. NeuroImage **30**(3), 813–826 (2006). DOI http://dx.doi.org/10.1016/j.neuroimage.2005.10.014
75. Wolters, C., Grasedyck, L., Hackbusch, W.: Efficient computation of lead field bases and influence matrix for the FEM-based EEG and MEG inverse problem. Inverse Problems **20**(4), 1099–1116 (2004). DOI http://dx.doi.org/10.1088/0266-5611/20/4/007
76. Wolters, C., Köstler, H., Möller, C., Härtlein, J., Grasedyck, L., Hackbusch, W.: Numerical mathematics of the subtraction method for the modeling of a current dipole in EEG source reconstruction using finite element head models. SIAM J. on Scientific Computing **30**(1), 24–45 (2007). DOI http://dx.doi.org/10.1137/060659053
77. Zhang, Y., Ding, L., van Drongelen, W., Hecox, K., Frim, D., He, B.: A cortical potential imaging study from simultaneous extra- and intracranial electrical recordings by means of the finite element method. Neuroimage **31**(4), 1513–1524 (2006)
78. Zhang, Y., van Drongelen, W., Kohrman, M., He, B.: Three-dimensional brain current source reconstruction from intra-cranial ECoG recordings. NeuroImage **42**(2), 683–695 (2008). DOI 10.1016/j.neuroimage.2008.04.263.

URL http://www.sciencedirect.com/science/article/B6WNP-4SGKBB4-3/2/be9c5075b633a57b111b633e3203b58b
79. Zienkiewicz, O.C., Taylor, R.L., Zhu, J.Z.: The Finite Element Method. Its basis and fundamentals. Elsevier Butterworth-Heinemann, Amsterdam [u.a.] (2005)